Improved characterization of the 3D structure of salt diapirs with electrical resistivity models

Filbandi Kashkouli, Mohammad; Comeau, Matthew J.; Kamkar-Rouhani, Abolghasem; Arab-Amiri, Alireza

DOI
10.1016/j.pepi.2025.107457

Publication date
2025

Document Version
Final published version

Published in
Physics of the Earth and Planetary Interiors

Physics of the Earth and Planetary Interiors 368 (2025) 107457

Contents lists available at ScienceDirect

Physics of the Earth and Planetary Interiors

journal homepage: www.elsevier.com/locate/pepi

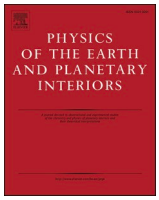

Improved characterization of the 3D structure of salt diapirs with electrical resistivity models

Mohammad Filbandi Kashkouli [a,*], Matthew J. Comeau [b,*], Abolghasem Kamkar-Rouhani [a], Alireza Arab-Amiri [a]

[a] Department of Mining, Petroleum and Geophysics, Shahrood University of Technology, Shahrood, Iran
[b] Department of Geoscience and Engineering, Delft University of Technology, Delft, the Netherlands

ARTICLE INFO

Keywords:
Magnetotelluric
Resistivity
Salt
Diapir
Tectonics

ABSTRACT

Salt diapirs are prominent geological features, formed by the piercing of buoyant salt within overlying strata, with implications for basin evolution, tectonic deformation, and resource accumulation. In this study, we investigate the Shurab salt diapirs in northwestern Central Iran—an area with five known near-surface diapirs—whose subsurface geometries and interconnections at depth remain unclear due to the complex structural settings. To address these challenges, we generated a 3D electrical resistivity model from an array of 183 magnetotelluric (MT) measurements. Phase tensor and resistivity phase tensor analyses confirmed the presence of multidimensional conductivity structures. A range of modeling tests were performed to ensure a robust result, and final models were validated against seismic data and borehole logs, as well as previous 2D electric modeling. The resulting 3D resistivity model provides new insight into the geometry, depth, and interconnectedness of the salt diapirs and superior resolution of diapir flanks compared to seismic data. High resistivity zones at shallow depths correspond to dry salt, while lower resistivity at greater depths indicates brine-saturated regions. Notably, Diapirs No. 4 and 5 were found to be interconnected at depth, sharing a root zone and likely originating from a common evaporite layer. Tectonic analysis suggests that active fault systems—including the Sen-Sen, Ab-Shirin, and Dehnar faults—have played key roles in guiding salt migration and shaping diapir structures. This study highlights the effectiveness of using MT data to image complex salt structures and underscores the importance of integrated geophysical approaches in tectonically active regions.

1. Introduction

Salt diapirs are unique geological structures formed by the movement and displacement of salt masses beneath the Earth's surface (e.g., Warsitzka et al., 2015; Gou and Liu, 2024). This phenomenon occurs primarily due to the physical properties of salt, such as its low density compared to the surrounding rocks and high deformability. The salt layers transformed into salt diapirs typically originate from evaporite deposits (e.g., Alsop et al., 2012; Jackson and Hudec., 2017) which were created by the evaporation of ancient saline waters. Over time, a number of effects, including the pressure from overlying sedimentary layers, causes the salt layer to deform and appear to migrate upward, forming structures like salt domes, salt pillars, or salt curtains (Gou and Liu, 2024).

Salt tectonics shapes regional tectonic and sedimentary frameworks. Diapirs, typically composed of lower-density materials like salt or gypsum, move upward toward the surface under tectonic pressure (Jackson and Hudec, 2017). This process can influence the formation of fold structures, causing changes in their shape and distribution, while thrust faults can push diapirs upward. These interactions lead to the development of unique features such as doubly-plunging folds and diapiric domes, contributing to the formation of mineral deposits and distinctive tectonic patterns in these regions (in the Pyrenean and Carpathian regions, for example, Santolaria et al., 2014; Stefanescu et al., 2000). Such studies highlight the dual role of diapirs as both active geological agents and passive markers of tectonic stress. Additionally, these features have implications for regional fluid dynamics and mineral deposition, further emphasizing their geological importance (e.g. Wu et al., 2016).

The study of salt diapirs also advances fundamental geological knowledge. Their dynamic evolution, from initial formation to eventual deformation under tectonic stress, offers a natural laboratory for

* Corresponding authors.
E-mail addresses: kashkoulimohammad@gmail.com (M. Filbandi Kashkouli), M.J.Comeau@tudelft.nl (M.J. Comeau).

https://doi.org/10.1016/j.pepi.2025.107457
Received 3 July 2025; Received in revised form 30 September 2025; Accepted 1 October 2025
Available online 3 October 2025

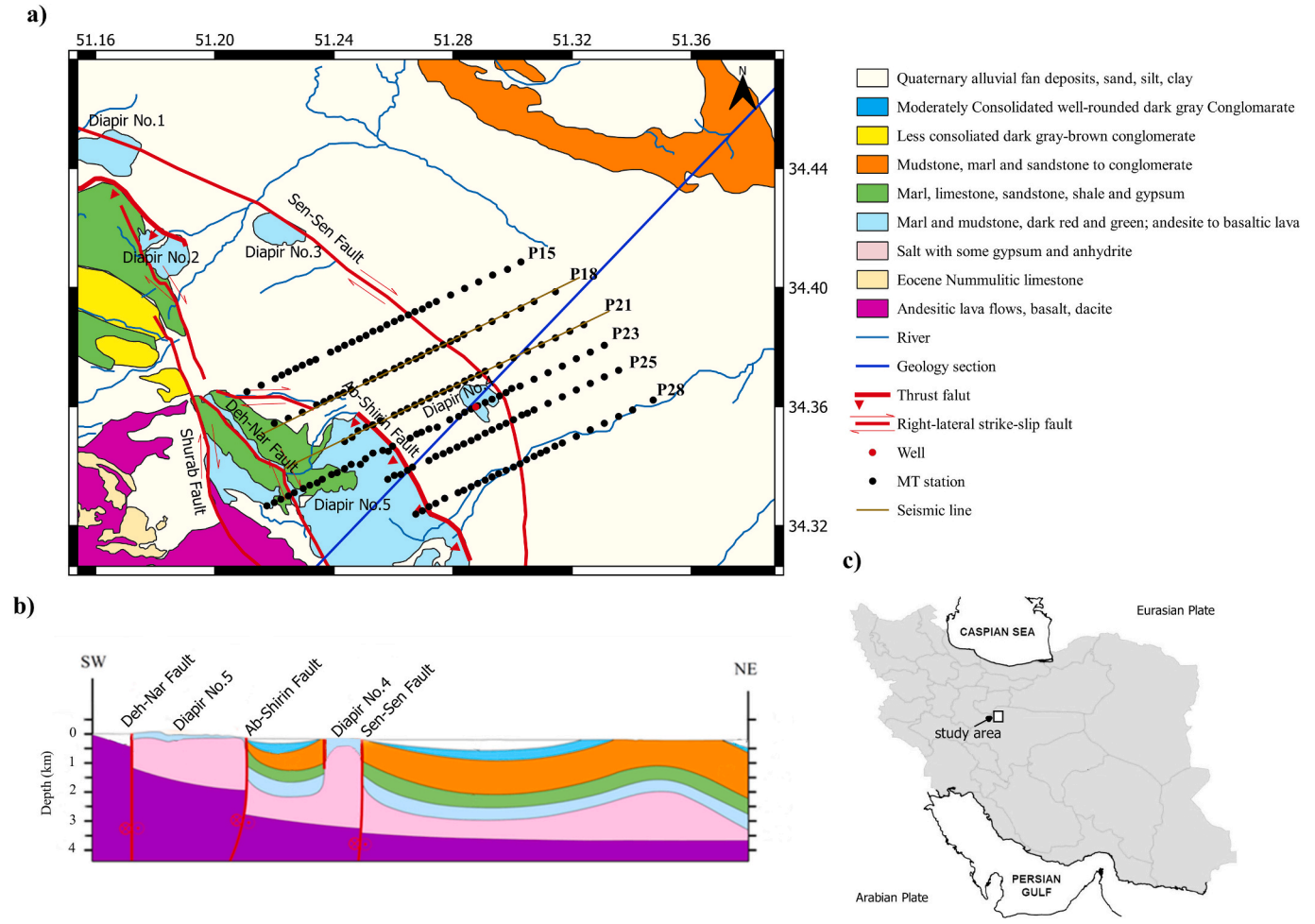

Fig. 1. (a) Map of the Shurab area with geological units (modified from Moradi et al., 2019). (b) Geological cross section across Diapir No. 4 and Diapir No. 5 (redrawn from Moradi et al., 2019). (c) Location of study area in the Central Iran.

understanding broader processes such as crustal deformation, sedimentary basin evolution, and fluid migration (Jackson et al., 2015; Henke et al., 2020). Comparative studies across global diapir provinces further enrich our understanding of these processes.

Salt diapirs play a pivotal role in basin dynamics, influencing sediment deposition and creating favorable conditions for hydrocarbon accumulation. Their ability to pierce overlying strata makes them prime sites for traps that can house oil and gas reserves, as observed in regions such as the Santos Basin and Gulf of Mexico (Mrlina and Beránek, 2024; Zhdanov et al., 2011). The complex interplay of buoyancy, tectonics, and sediment loading drives their formation, with each factor contributing to the diversity of diapir geometries across different basins. Understanding these dynamics is crucial for optimizing hydrocarbon exploration strategies.

Salt diapirs are increasingly recognized for their environmental and industrial applications. Their impermeable nature and stability under pressure make them ideal for storing hazardous materials, including radioactive waste and CO_2 (e.g., Van gent et al., 2011; Teofilo et al., 2016). An understanding of internal deformation and stress distributions ensure their safe use in such contexts, and these geomechanical analyses must start with proper definition of the boundaries and geometry of the salt structures.

The study of salt diapirs integrates insights into tectonic processes, resource exploration, and environmental applications, showcasing their interdisciplinary importance. However, accurate imaging of salt diapirs, especially those with very complex structures, remains a huge challenge (e.g. Davison et al., 2013).

Advancements in geophysical imaging have significantly improved the characterization of salt diapirs. Methods such as seismic reflection (Leveille et al., 2011; Jones and Davison, 2014; Montazeri et al., 2020), magnetotellurics (MT) (den Boer et al., 2000; Key et al., 2006; Aleksanova et al., 2009; Rubinat et al., 2010; Baikpour et al., 2016; Moradi et al., 2019; Henke et al., 2020; Filbandi Kashkouli et al., 2025), and gravity modeling (e.g., Pinto et al., 2005; Mrlina and Beránek, 2024) have been used to glean information about these complex structures. For example, both 3D seismic reflection data and MT data have provided detailed insights on the possible structures, such as anticlines, synclines, and boudinage, in the Zechstein and North Sea salt systems (Van Gent et al., 2011; Avdeeva et al., 2012). However, some methods can struggle in certain environments to accurately define salt diapirs, such as the seismic reflection method that is ineffective in delineating overhangs and steeply dipping salt flanks (Avdeeva et al., 2012; Zhdanov et al., 2011). Geophysical imaging methods, and their combination (Henke et al., 2020; Filbandi Kashkouli et al., 2025), can help resolve features that traditional geological and structural mapping miss, enabling better predictions of diapir behavior and associated risks.

1.1. Study aim

Our research focuses on the Shurab salt diapirs, situated in the northwestern region of Central Iran. This area, part of the Great Kavir Desert that is characterized by an arid climate with minimal rainfall and high surface evaporation, is home to five salt diapirs. Their locations are known from geological surface mapping. Their subsurface geometries

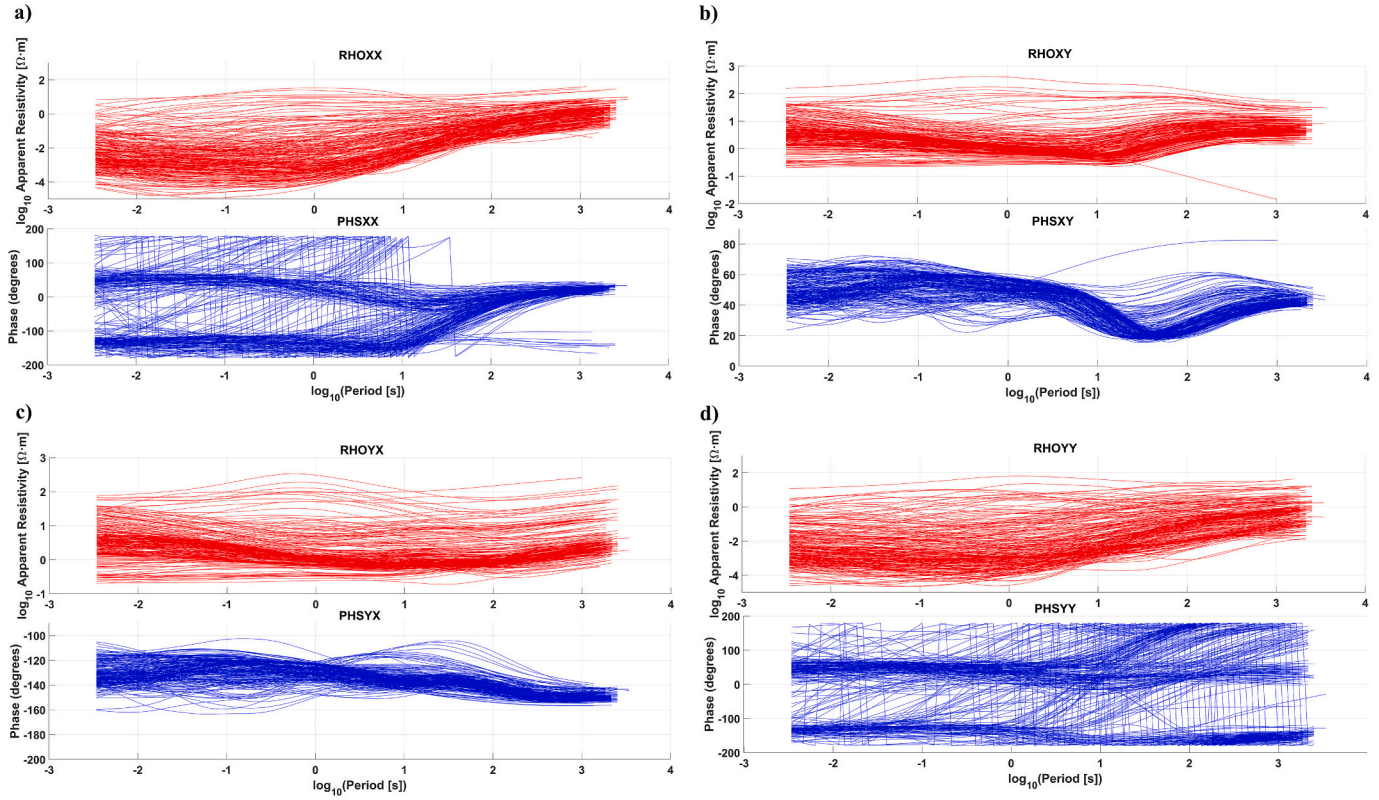

Fig. 2. Observed apparent resistivity (top row) and impedance phase (bottom row) for each impedance components (a–d; Z_{xy}, Z_{xx}, Z_{yx}, and Z_{yy}).

and interconnections at depth are not well understood due to the complex structural and tectonic characteristics associated with these diapirs. These complexities arise from their interactions with nearby fault systems and pull-apart extensional structures, which result in intricate deformation and compartmentalization (Morley et al., 2009; Arian, 2012; Baikpour et al., 2016). Furthermore, the physical connections between these diapirs contribute additional layers of complexity, making it challenging to fully interpret their subsurface geometry (Moradi et al., 2019).

Seismic data acquired in the area have failed to provide clear boundaries for the diapirs, primarily due to poor resolution and the inherent difficulties of imaging steeply inclined or overhanging geological formations (Davison et al., 2013; Baikpour et al., 2016). Simplified 2D modeling of MT data improved the understanding of these features, determining the locations, diameters, and depths (Filbandi Kashkouli et al., 2025). However, the full 3D structure and complex geometry of the diapirs across the region remained unknown.

Full 3D modeling provides a powerful tool for imaging and interpreting subsurface structures with greater accuracy and resolution. In the context of salt tectonics, it enables the visualization of complex spatial relationships between salt diapirs and surrounding geological features, such as fault zones and adjacent diapirs. Unlike a 2D approach, which may oversimplify subsurface geometries due to limited perspective, full 3D modeling captures the true three-dimensional shape and extent of these bodies. Ideally, it can highlight how individual diapirs are connected at depth, whether through feeder systems, welds, or intervening salt sheets, and how fault systems may have influenced or been influenced by salt movement.

In this study, we aim to address how 3D modeling can provide a more accurate understanding of the structure and geometry of salt diapirs and, specifically, how it can reveal information about their interconnections, in essence, revealing the nature of their roots. To do this we generate a three-dimensional electrical resistivity model using data from an array of 183 MT measurements across the area.

2. Geological background

The Shurab region is located in the eastern part of the Central Iran Block and forms a segment of the Urumieh-Dokhtar magmatic belt (Sonder, 1954). This belt, which resulted from tectonic activities following the closure of the Neo-Tethys Ocean, is characterized by extensive volcanism and the intrusion of igneous bodies during the Eocene (Berberian and King, 1981). The tectonic setting of the area has significantly influenced its geological evolution, with magmatic activity, structural deformation, and tectonic events playing pivotal roles (e.g., Morley et al., 2009). The region's position along the eastern margin of the Central Iranian Plateau and its proximity to major fault systems have contributed to the development of complex structural features such as anticlines, strike-slip faults, and salt domes (e.g., Morley et al., 2009).

From a stratigraphic perspective, the Shurab area exhibits considerable lithological diversity. The Eocene volcanic units, composed of intermediate to acidic volcanic rocks, constitute the geological basement of the region (Sonder, 1954). Overlying these units is the Qom Formation (QF), with a thickness exceeding 1200 m, consisting of limestone, marl, and evaporitic layers, deposited during the Oligocene to Miocene. Lithologically, this formation includes various zones of carbonate rocks, colored marls, and salt evaporites, indicative of a shallow, evaporitic depositional environment (e.g., Reuter et al., 2007; Furrer and Suder, 1955). Beneath the QF lies the Lower Red Formation (LRF), approximately 1000 m thick, comprising alternating layers of gypsum, anhydrite, and other evaporitic rocks consistent with the environmental conditions of hot, arid marginal sedimentary basins. Above the QF is the Upper Red Formation (URF), which is subdivided into two distinguishable units: the lower evaporitic unit, consisting of anhydrite and marl, and the upper unit, composed of red and light yellow sandstone and marl. This stratigraphic diversity reflects a complex history of sedimentation over various geological periods in response to climatic changes, tectonic activity, and basin evolution. A simplified geological map of the Shurab area is shown in Fig. 1.

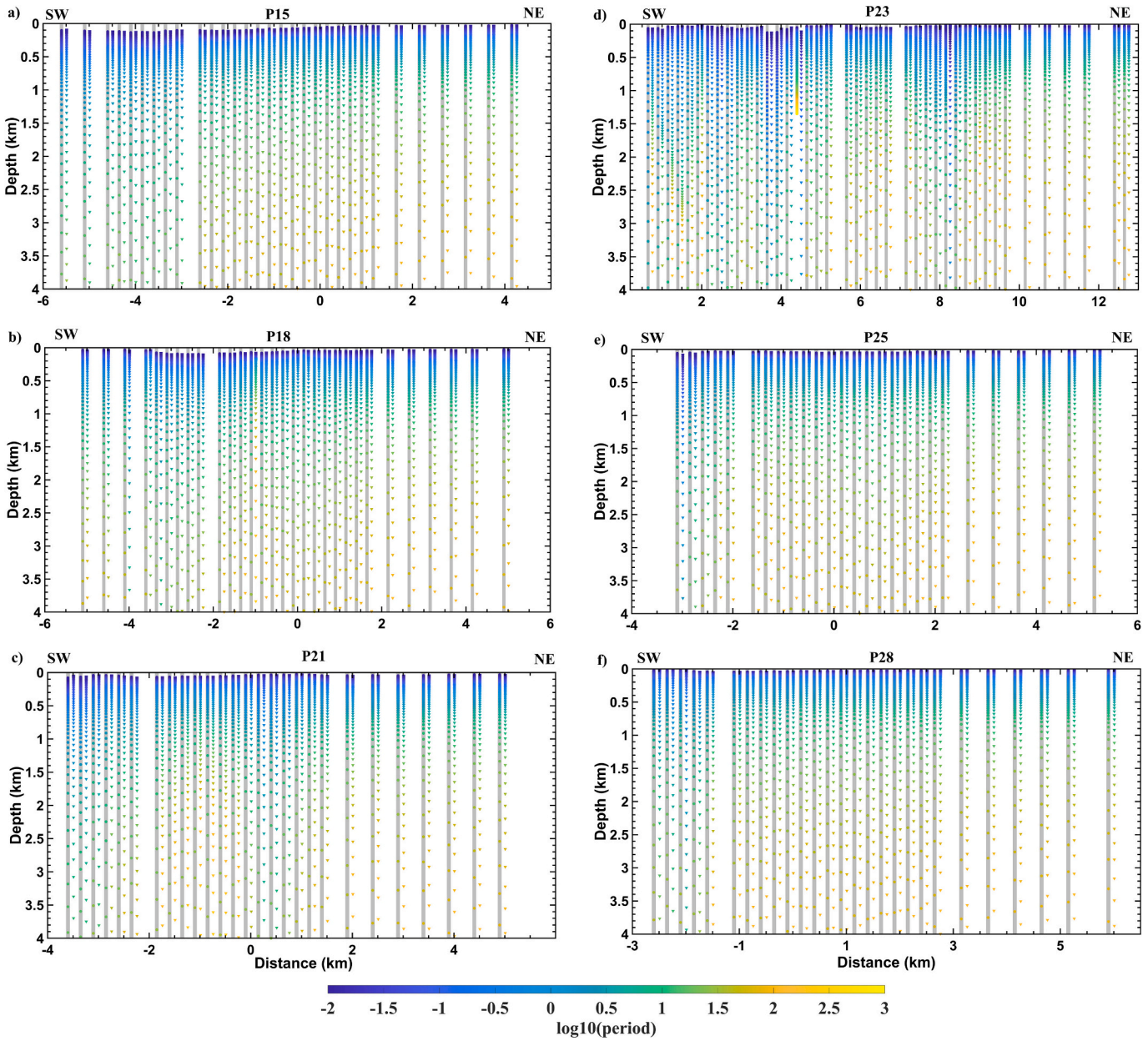

Fig. 3. Depth estimation using the Niblett–Bostick transformation in TE and TM modes for six profiles: 15, 18, 21, 23, 25, and 28 (a–f). Left columns is for TE mode and right is for TM mode.

3. MT data

MT data comprise surface measurements of the horizontal electric and magnetic fields, which are related through an impedance tensor (Z) that reflects the subsurface electrical resistivity structure of the Earth (e.g., Berdichevsky and Dmitriev, 2008). Variations in the fields arise from natural sources, including interactions between the solar wind and the Earth's magnetosphere and ionosphere and activity in the atmosphere from worldwide lightning discharges (e.g., Unsworth and Rondenay, 2012). Apparent resistivity and impedance phase are derived across a wide range of frequencies, giving sensitivity to multiple spatial scales: the higher frequencies (i.e., shorter periods) provide information about shallower depths and the lower frequencies (i.e., longer periods) probe deeper structures.

In 2013, MT data were collected within the study area in the form of an array consisting of six profiles. The measurement sites were spaced approximately 200 m apart along each profile, with a profile-to-profile separation distance of 1500 m. The instrument used for data acquisition was the MTU V5–2000 from Phoenix Geophysics, Canada. The perpendicular horizontal electric field components and magnetic field components were measured. In addition, the vertical magnetic field was recorded at some locations (approximately every second or third site), to provide induction vector or tipper data. The recorded data, shown in Fig. 2, covered a range from 0.0033 s (~300 Hz) to 2500 s.

To estimate the maximum depth of electromagnetic penetration at each site along each profile, we applied the Niblett–Bostick depth approximation method (Niblett and Sayn-Wittgenstein, 1960; Bostick, 1977; Jones, 1983). The validity of this approach relies on the prerequisite that the impedance tensor can be accurately decoupled into transverse electric (TE) and transverse magnetic (TM) modes, and that both modes exhibit equivalent penetration depths under the assumption of 1D conductivity structure. The resulting penetration depth estimates for the TE and TM modes at each site are presented in Fig. 3 and in Fig. S1 in the Supplementary Material file. The penetration depths

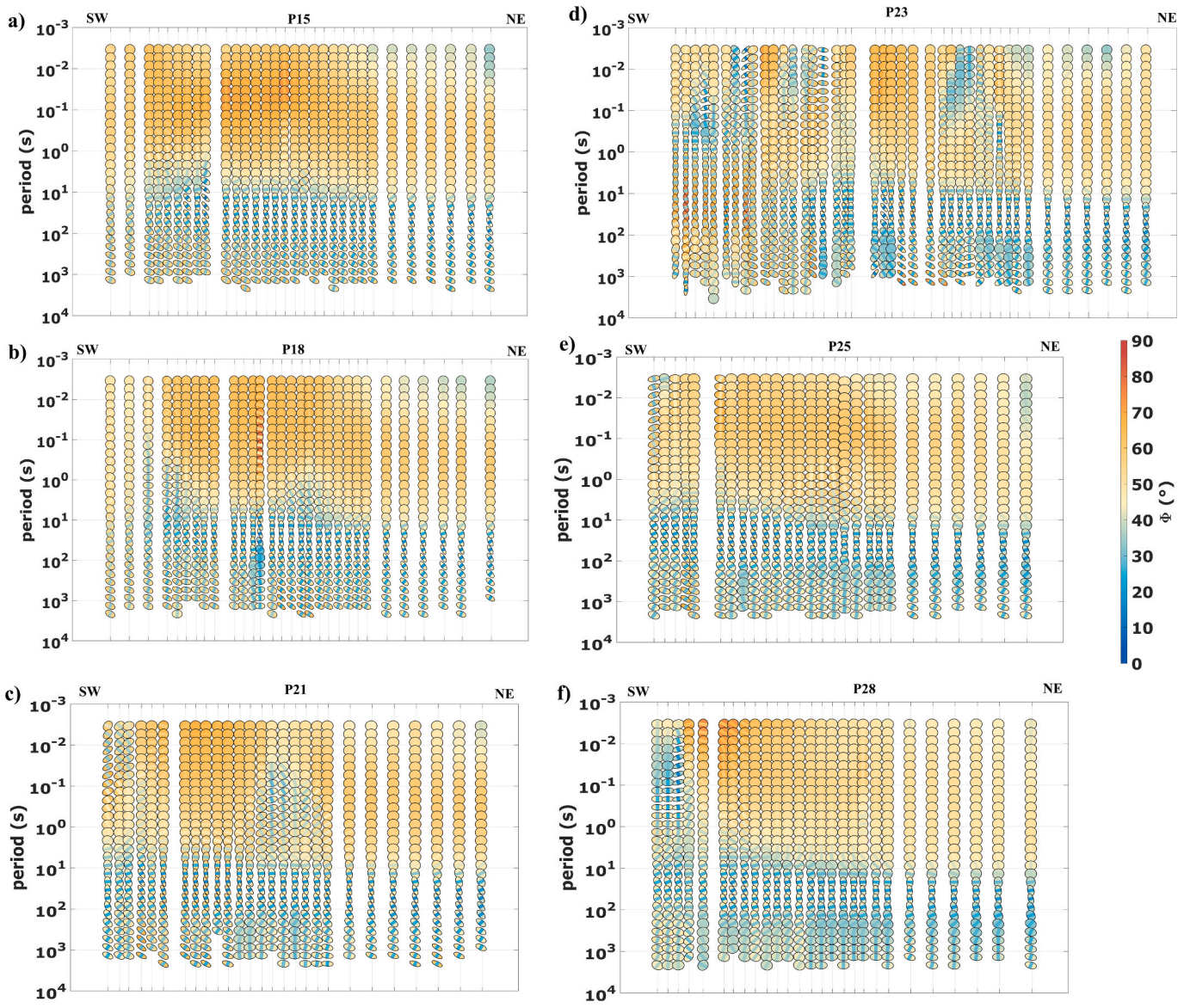

Fig. 4. Phase tensor ellipse pseudo-sections shown as six profiles (a–f). The ellipses are color-filled to represent ϕ_{max} with a colored bar indicating ϕ_{min}.

exceed 20 km at nearly all sites.

3.1. Phase tensor and resistivity phase tensor analysis

Before carrying out modeling of the collected data through a non-unique inversion processes, it is crucial to carefully analyze the data (e.g., Booker, 2013). This study utilizes the phase tensor (PT) (Caldwell et al., 2004) and resistivity phase tensor (RPT) (Hering et al., 2019).

The PT, a second-rank tensor, encapsulates the phase relationships between the horizontal electric and magnetic field components in MT data (Caldwell et al., 2004). It is particularly valuable in 3D settings, as it retains regional phase information despite (galvanic) distortions from near-surface conductivity variations. The PT is characterized by three coordinate-invariant parameters: the maximum (ϕ_{max}) and minimum (ϕ_{min}) principal values and the skew angle (β). The principal values quantify the tangent of phase differences between the electric and magnetic fields along the principal axes, while the skew angle indicates the dimensionality of the conductivity structure. The orientation of the PT's principal axes, given by the angle α, reveals the strike direction of the conductivity structure. It is often represented graphically as an ellipse.

When ϕ_{min} exceeds 45°, it suggests the possible presence of subsurface conductors (Caldwell et al., 2004; Bibby et al., 2005). In the survey area, we observe that at most measurement sites, periods of less than approximately 3 s display ϕ_{min} values greater than 45°, and periods greater than approximately 10 s display ϕ_{min} values less than 45°, indicating a transition from a near-surface conductive layer to a deeper non-conductive zone (e.g., the basement) (see Fig. 4). However, it is notable that this simple layered structure is broken at certain locations along the profiles when this transition occurs at shorter periods (e.g., profile 18 at a distance of −2 km and period of 0.3 s and 1 s). This indicates an anomalous (resistive) feature in an otherwise horizontally layered subsurface.

The RPT is derived from the complex apparent resistivity tensor and quantifies the phase relationships between the observed electric field and the apparent current density (Brown, 2016; Hering et al., 2019). This makes the RPT sensitive to vertical resistivity gradients, providing a more nuanced understanding of subsurface structures. The RPT is also free from static distortions under the same conditions as the PT. In fact, the RPT exhibits a higher sensitivity to resistivity contrasts compared to the PT (Hering et al., 2019). This is especially true in anisotropic and multidimensional environments. For instance, in 1D isotropic models,

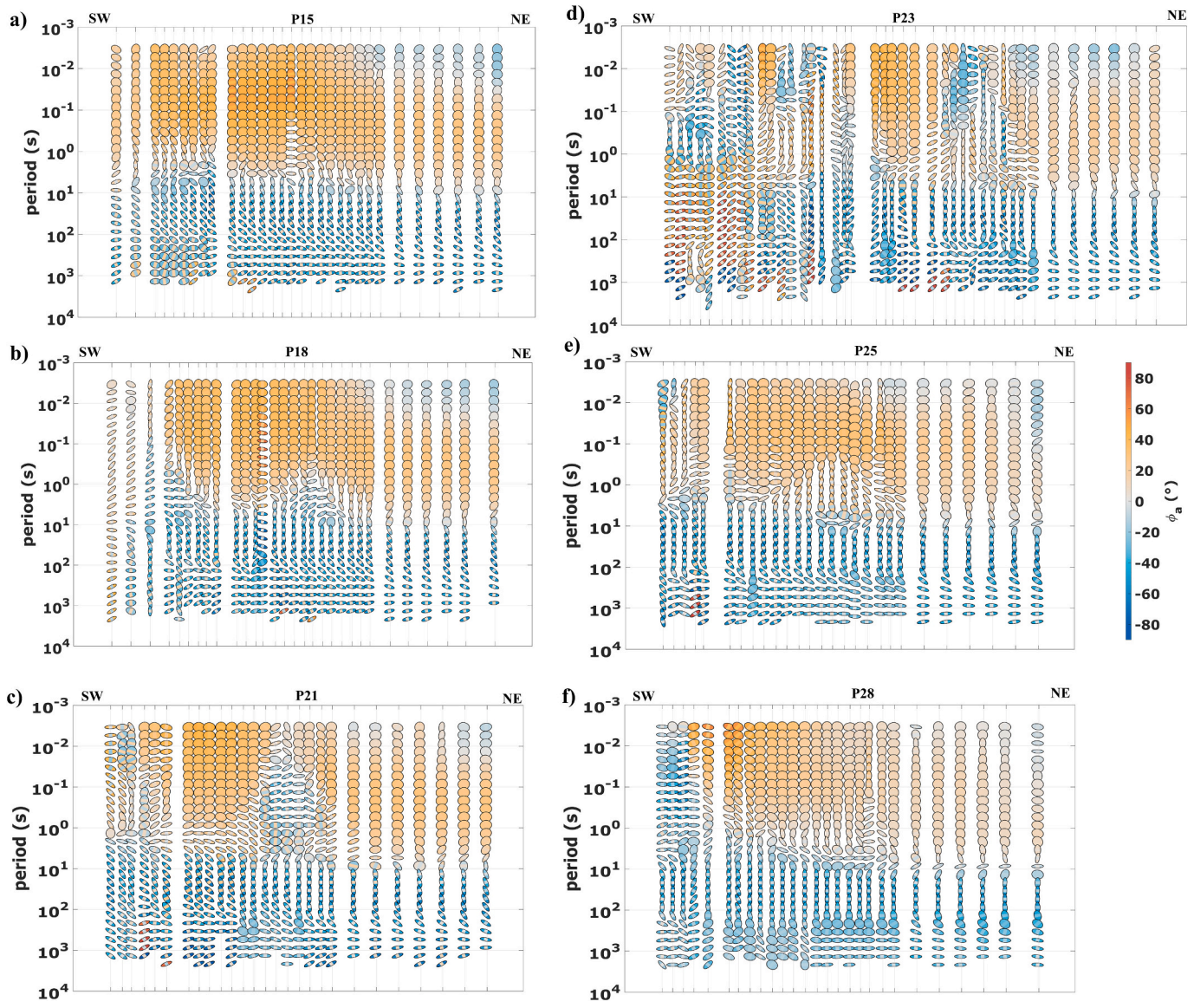

Fig. 5. Frequency-dependent resistivity phase tensor (RPT) pseudo-sections derived from the MT array data are shown for six profiles (a–f). Each ellipse is filled with a color indicating the value of the major axis, while a colored bar represents the minor axis. Significant features are directly observable within the data.

the RPT shows steeper gradients and larger amplitude variations, which can improve the resolution of thin conductive layers (Hering et al., 2019). In anisotropic environments, the RPT aligns with the principal axes of anisotropy, providing clear insights into the direction and magnitude of resistivity changes. In 2D and 3D environments, the RPT is highly responsive to vertical boundaries and associated charges, making it a valuable tool for identifying horizontal resistivity gradients (Hering et al., 2019).

For 1D structures, the principal axes of the RPT satisfy $\phi_{a,max} = \phi_{a,min}$, and the tensor is represented by a circle (Hering et al., 2019). For 2D structures, two distinct modes exist: one where α=0°and β=0°, and another where α=90° and β=0°. Here, β represents the orientation of the major axis relative to a reference axis, while α defines the position of the reference axis relative to the coordinate axes.

The results of the RPT analysis are presented in the Fig. 5. For periods less than 1 s, the data are 1D and 2D across all measurements. For periods in the range of 1–10 s there is the start of a transition and for periods of 10–100 s the data are indicated to be 3D. For periods greater than 100 s, the data are 2D and 3D across all measurements. In these period intervals, where a transition has occurred, sub-surface anomalous features are anticipated.

Vertical and layered variations in resistivity are not distinctly observed in the PT sections. In contrast, the RPT sections—due to their sensitivity to vertical resistivity variations—clearly reveal vertical stratification and associated resistivity changes. In the PT sections, it is possible to distinguish two layers: one smaller than approximately 3 s and another greater than 10 s. However, in the RPT sections, several layers can be well distinguished based on their values and shapes. One layer appears in the time window of less than 1 s, characterized by positive values exceeding 40 degrees. In the 1–10 s range—particularly in the central and southwestern parts of the profiles—RPT values become negative, indicating 3D structures. In the 10–100 s range, another mainly 3D structure is observed, and beyond 100 s, yet another distinct 3D structure is present.

4. 3D data modeling

In this study, MT data within the study area were inverted using the ModEM code (Egbert and Kelbert, 2012; Kelbert et al., 2014), producing a 3D electrical resistivity model. This inversion algorithm can handle

Table 1
Model parameters for each inversion test.

Test Number	Core mesh dimension (m)	Initial model resistivity (Ωm)	Covariance	Data type	Iterations	nRMS starting	nRMS final
1	165*165	1	0.5	Impedance	92	5.71	1.28
2	165*165	3	0.5	Impedance	71	6.80	1.34
3	165*165	10	0.5	Impedance	76	15.8	1.30
4	165*165	30	0.5	Impedance	100	32.6	1.18
5	165*165	3 / 30 (2-layer)	0.5	Impedance	69	8.13	1.29
6	165*165	3 / 1 / 3 / 10 (4-layer)	0.5	Impedance	79	5.42	1.21
7	165*165	3	0.2	Impedance	92	6.80	1.37
8	165*165	3	0.3	Impedance	85	6.80	1.27
9	165*165	3	0.4	Impedance	92	6.80	1.13
10	165*165	3	0.5	Impedance	71	6.80	1.39
11	165*165	3	0.6	Impedance	77	6.80	1.43
12	165*165	3	0.7	Impedance	80	6.80	1.69
13	165*165	3	0.5	Off-diagonal impedance	63	4.72	1.04
14	165*165	3	0.5	Impedance	71	6.80	1.34
15	165*165	3	0.5	Tipper	62	8.24	2.26
16	165*165	3	0.5	Impedance+tipper	76	4.89	1.57
17	165*165	3	0.2	Phase tensor	69	6.23	2.07
18	165*165	3	0.3	Phase tensor	68	6.23	2.01
19	165*165	3	0.5	Phase tensor	64	6.23	2.25
20	165*165	3	0.7	Phase tensor	66	6.23	2.56
21	100*100	3	0.6	Phase tensor	40	6.23	2.62
22	100*100	3	0.5	Impedance	83	6.82	1.12
23	100*100	3	0.6	Impedance	69	6.82	1.28
24	100*100	3	0.7	Impedance	69	6.82	1.38

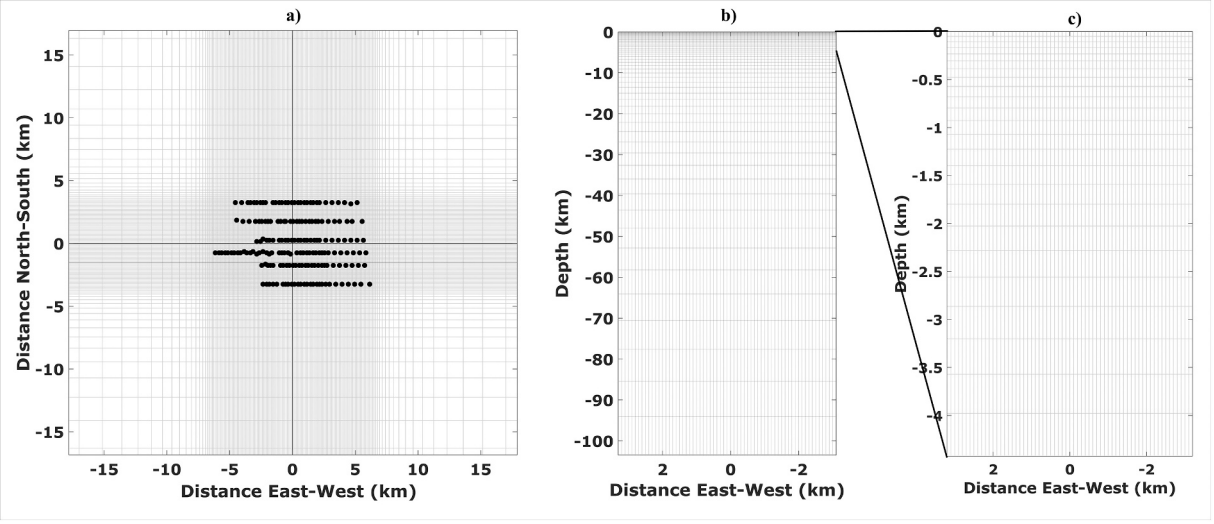

Fig. 6. Figure panels show the discretization of the 3D modeling mesh: a plan view (a) and two vertical cross-sections (b and c) presented at different scales. Black circles in the plan view denote the positions of MT measurement sites.

different types of data. We tested different data types including the full impedance tensor, the off-diagonal components of the impedance tensor only, the full impedance tensor jointly with tipper data, tipper data only, and phase tensor data (see Fig. S2 in the Supplementary Material file for testing of the data type). Since the objective of this study is to focus on depths up to 4000 m, data with periods ranging from 0.0033 s to 1090 s were selected for modeling. In addition to testing different data types, we tested various modeling parameters including the covariance parameters for smoothing and the initial model (Table 1).

With regards to selecting an initial model, we tested homogeneous half-space models (with resistivity values of 1, 3, 10, and 30 Ωm), as well as two- and four-layer models based on a 1D model generated from the data (see Hersir et al., 2013; Comeau et al., 2021; Robertson et al., 2020). The results of these tests indicated that a homogeneous half-space with a resistivity of 3 Ωm was the most suitable initial model (see Fig. S3 in the Supplementary Material file for testing of the initial model).

The model covariance parameter, a value between 0 and 1, is effectively a trade-off between a smooth and a rough model (see Robertson et al., 2020; Comeau et al., 2021). The covariance parameter was varied from 0.2 to 0.7. Although it did have an influence on the final model result, the main structures remained consistent. With regards to the covariance parameters, we found a value of 0.6 was ultimately preferred for both the horizontal and vertical directions (see Figs. S4 in the Supplementary Material file for testing of the covariance parameter).

Modeling of different data types produced remarkable similar models. Notably, modeling only the off-diagonal components of the impedance tensor or the full impedance tensor produced models with very similar structures and resistivity values. The phase tensor data also produced a very similar model. These tests give a good indication of the robustness of model features and the uncertainty in the modeling procedure. Overall, the tests described above suggest that the main structures and resistivities observed in the model are required.

To achieve the best fit between observed and predicted data, error

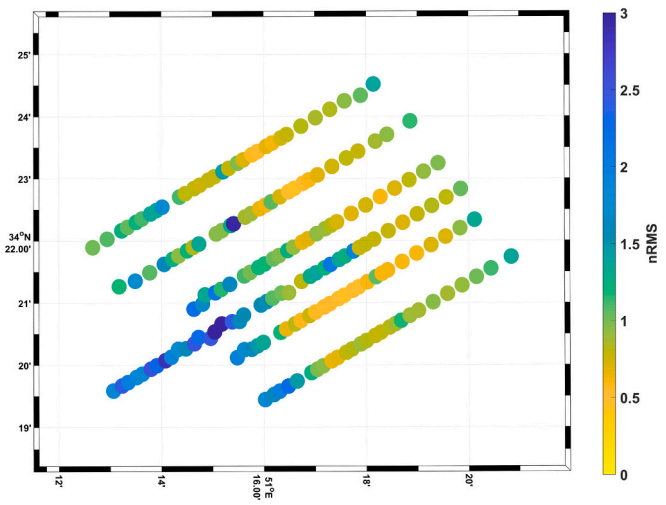

Fig. 7. Normalized root mean square (nRMS) misfit between observed and predicted data from the preferred model. Colored dots represent the misfit values at individual MT measurement sites. The overall nRMS is 1.28.

floor values were applied to the data. These were set as follows: 10 % of $\sqrt{|Z_{xy}||Z_{yx}|}$ to Z_{yy} and Z_{xx}, and 5 % of $\sqrt{|Z_{xy}||Z_{yx}|}$ to Z_{yx} and Z_{xy}. For tipper and phase tensor data, an absolute error floor of 0.05 was applied. We can then compute the root-mean-square (RMS) misfit, which is used as a criterion to determine overall model fit.

For the modeling grid, topography was not used because the terrain in the study area is relatively flat. The depths therefore represent depths below surface level (which is approximately 600 m above sea level). The site spacing ranged from 160 to 600 m. A rectangular modeling grid was designed for modeling. It was aligned with the profile directions (and the data were rotated accordingly). The modeling grid consisted of a central core area of interest and an outer area. Within the central core area of the final model, the horizontal cell size was 100 × 100 m^2, corresponding to approximately 25–30 % of the site spacing, a typical value (Robertson et al., 2020). The selected cell size for the central part of the model ensures numerical accuracy in the forward modeling. Moreover, it gives the model the ability to resolve fine structures. Outside the central core, 18 padding cells were added for computational stability of the inversion algorithm (Weaver, 1994), with a growth factor of 1.3. This configuration extends the model dimensions to approximately 120

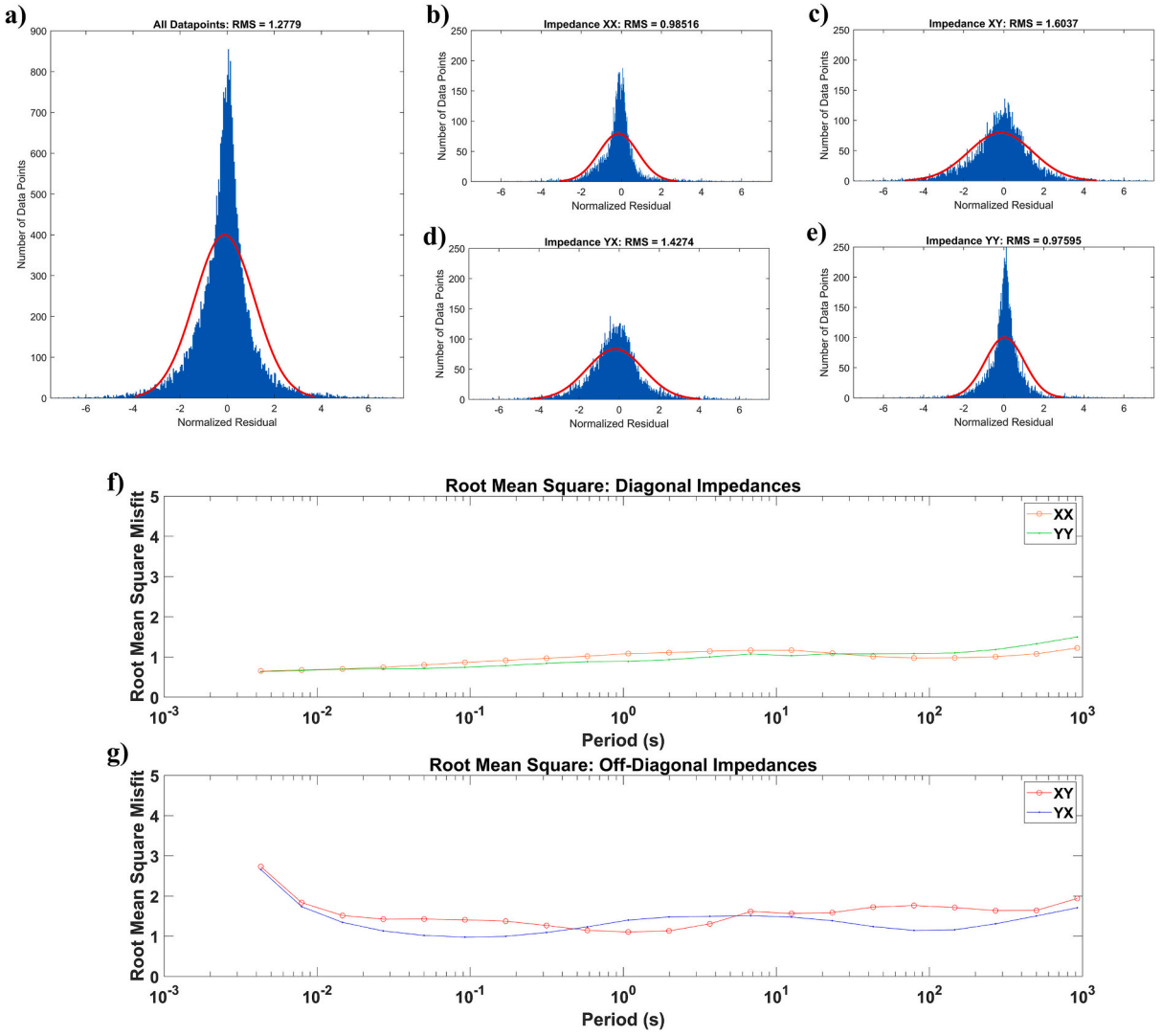

Fig. 8. Normalized root mean square (nRMS) misfit between the measured and calculated MT data from the preferred model. Panel (a) shows the normalized residual for all impedance components. Panel (b) and (e) show the normalized residuals for the diagonal impedance components (Z_{xx} and Z_{yy}) and panel (c) and (d) show the normalized residual for the off-diagonal impedance components (Z_{xy} and Z_{yx}). Panel (f) and (g) show the nRMS misfit as a function of period for the diagonal impedance components (Z_{xx} and Z_{yy}) and the off-diagonal components (Z_{xy} and Z_{yx}).

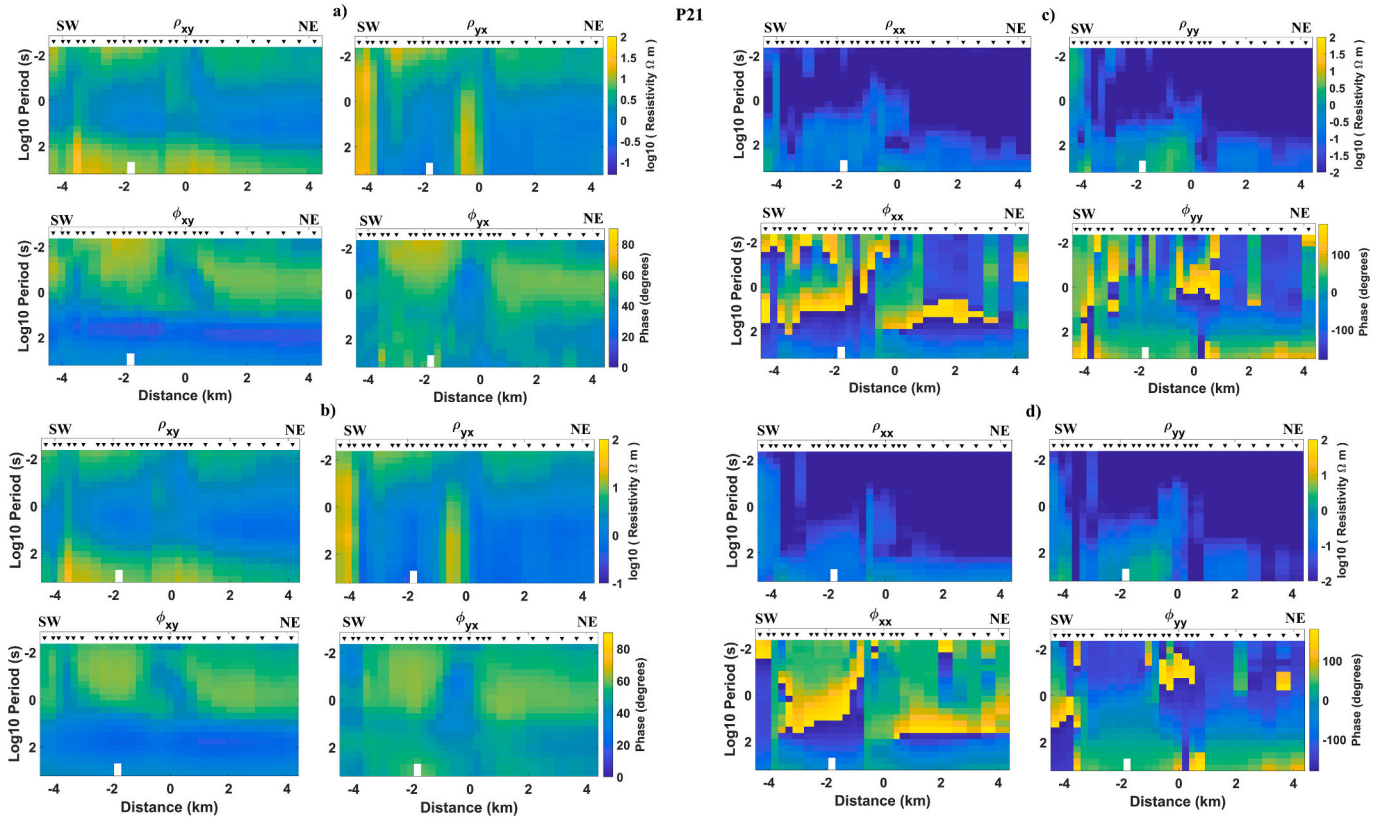

Fig. 9. Pseudo-sections of the observed data (top rows) and the preferred model response (bottom rows) for Profile 21. (a) Data and (b) model response for xy and yx (off-diagonal) components. (c) Data and (d) model response for xx and yy (diagonal) components. A comparison reveals a close and satisfactory fit between the two.

km in the horizontal directions.

In the vertical direction, the thickness of the grid cells smoothly increased with depth. Starting from an initial thickness of 50 m, they increased by a factor of 1.1, and extended to a total depth of approximately 120 km. The total number of cells in the x, y, and z directions is 120, 178, and 60, respectively. This implies that at the target depths of 1 km and 2 km, the maximum thickness of the cells is 140 m and 230 m, respectively, while at a depth of 4 km it is 410 m. This thickness ensures that the final model can effectively capture the detailed structures in the region. Note that in order to speed up the computations while testing various parameters (as above), the horizontal cell size was 165 m and the vertical increase factor was 1.2. Fig. 6 shows views of the modeling mesh discretization for 3D modeling. Fig. 6a presents a plan view of the mesh, while Fig. 6b and c display two different scales of the mesh in the vertical direction.

It is important to note that a low nRMS value does not necessarily indicate the suitability of an inversion result (e.g. Tietze et al., 2023; Comeau et al., 2021; Robertson et al., 2020; Grayver et al., 2013; Tietze and Ritter, 2013). Detailed comparisons between the measured and modeled data indicate that the models accurately represent both the diagonal and off-diagonal impedance components. Additionally, the quality of the fit is fairly uniform across all measurement sites, implying that no single site disproportionately affects the model. Likewise, the fit seems to be reasonably balanced across the different data components.

The final model selection for interpretation should be based on prior studies and the geological characteristics of the study area. Accordingly, we selected as the preferred model the model based on impedance data with a covariance value of 0.6 for our final interpretation. Fig. 7 shows the total nRMS values for each measurement site, and Fig. 8 displays the nRMS normalized residuals for each impedance component and the fit with period. A pseudosection of the data and the model along Profile 21 is shown in Fig. 9 (see Figs. S5–S10 in the Supplementary Material file for pseudosections of all data).

5. Discussion

5.1. General description of model results

The modeling results are shown in Fig. 10 as vertical sections along each profile, for the full impedance tensor model, which is the preferred model, as well as the phase tensor model and the off-diagonal impedance tensor model. Horizontal slices of the full impedance tensor model are shown in Fig. 11. Model sensitivity testing (Fig. S11) showed that the models are sensitive to features at depths of 2 km and 4 km, but lose sensitivity for depths of 10 km and 20 km.

To support the interpretation of the results, we examine a geological cross-section (Fig. 1b) that passes through the survey area, constructed using surface geological observations (see Moradi et al., 2019). Comparison between the resistivity models and the geological cross-section reveals that lithological variations are the primary controls on the observed resistivity contrasts. The geological cross-section indicates that the eastern portion of the study area is characterized by regularly bedded strata, reflecting minimal tectonic disturbance. In contrast, the western section exhibits a more complex geological architecture, shaped by tectonic deformation associated with the Sen-Sen, Ab-Shirin, and Deh-Nar faults.

Across the survey area, a near-surface layer with moderate to high resistivity (1–50 Ωm) is consistently observed, showing greater resistivity in the southwestern region compared to the northeast. This layer, ranging in thickness from 50 to 150 m, corresponds to Quaternary deposits and Pliocene conglomerates. Beneath it lies a very low resistivity layer (<1 Ωm), most prominent in the northeastern section, reaching up to 1000 m thick. This zone corresponds to highly saline mudstones and marly sandstones of the Miocene-aged Upper Red

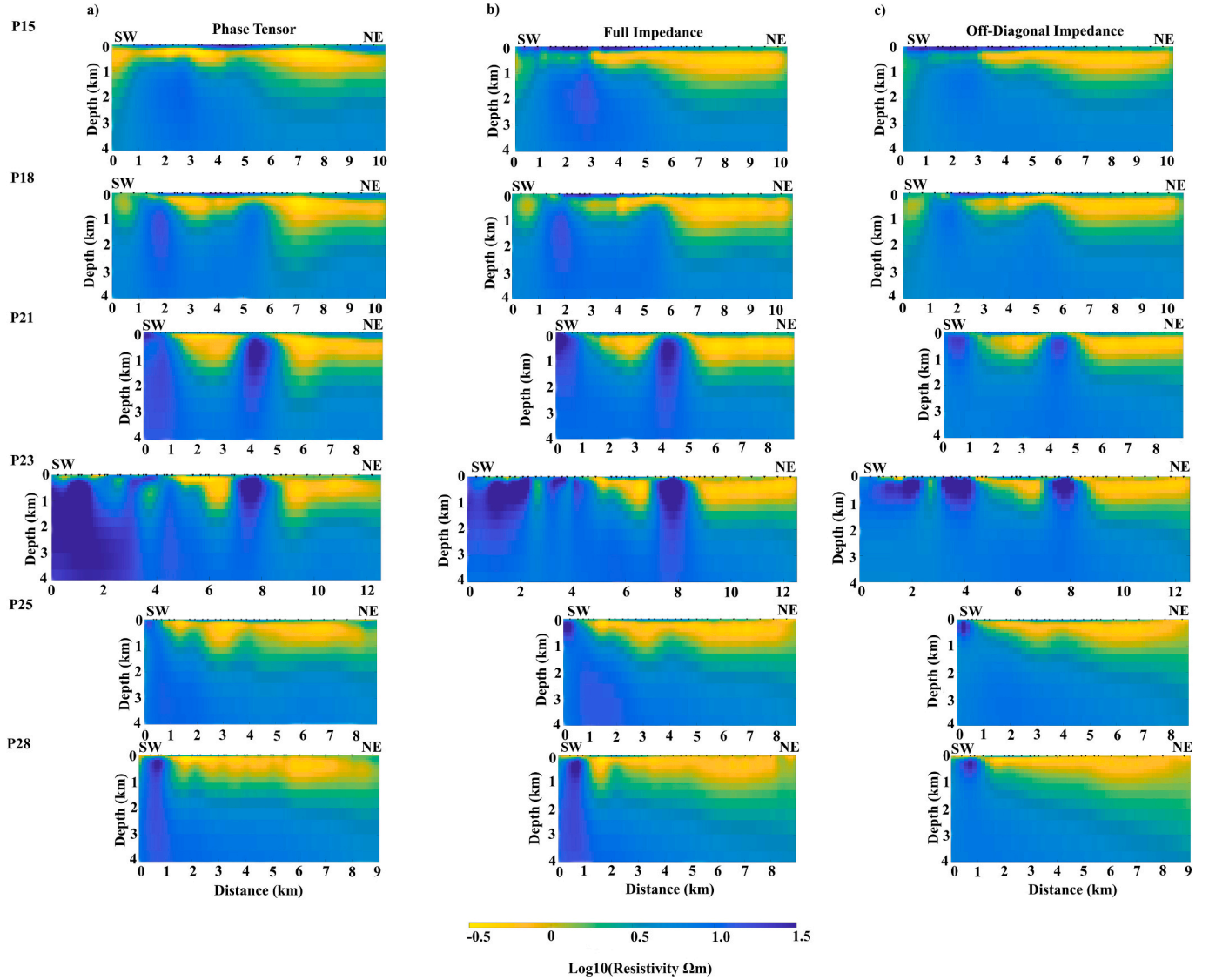

Fig. 10. Vertical sections from the resulting 3D electrical resistivity models along six profiles, Profiles 15, 18, 21, 23, 25, and 28 (rows) for the phase tensor model, the full impedance tensor model, and the off-diagonal impedance tensor model (columns).

Formation (URF). Below the URF, a layer of marly limestones and shaly sandstones from the Qom Formation (QF) exhibits moderate resistivity (<3 Ωm). Further below, a higher resistivity layer (3–30 Ωm) is attributed to the Lower Red Formation (LRF), composed of mudstone, marl, and anhydrite. This unit is significant as it hosts the region's salt diapirs, whose depths and configurations vary across profiles. The sharp contrast between the high-resistivity salt diapirs and surrounding low-resistivity sediments makes them ideal for electromagnetic imaging. At greater depths, a high resistivity zone (>30 Ωm) marks the presence of Eocene volcanics and older basement rocks. The transition to this basement is gradual in the models and occurs at depths ranging from approximately 1 km in the southwest to about 3 km in the northeast, aligning well with the known geological structure of the area.

5.2. Roots and interconnection of diapirs No. 4 and 5

As shown in Figs. 10 and 11, the diapirs exhibit high electrical resistivity at depths shallower than 3 km due to the dry nature of the salt. At greater depths, however, they display low electrical resistivity, which is attributed to interconnected pores and permeability associated with saline brines (e.g. Lewis and Holness, 1996; Henke et al., 2020). Fig. 12 presents the 8 Ωm isosurface, delineating the interconnection between the two diapirs and revealing their underlying roots. The isosurface reveals a prominent zone of morphological continuity between the two main diapiric structures, suggesting a potential interconnection at depth. This could represent either a sedimentary or structural bridge formed by deformation between the rising salt masses or the result of coalescence of two originally separate diapirs due to lateral salt flow. The geometry implies a phase of convergent diapirism or mutual influence during ascent. The tapering of both diapir roots into a common depth horizon supports the interpretation that both bodies may originate from a shared evaporite layer. This observation aligns with regional models of salt tectonics, where an extensive autochthonous salt layer feeds multiple diapiric intrusions. The merging roots also suggest a highly mobile salt layer capable of flowing laterally to support multiple piercement structures. The root morphology of the diapirs—narrow, deep-reaching features that appear to converge—suggests focused vertical salt flow, possibly through pre-existing zones of weakness such as faults or fractures. The absence of lateral broadening at the base implies a relatively confined source zone, potentially indicative of localized loading or differential sedimentation as the primary diapirism trigger. The spatial arrangement and interconnection between the diapirs

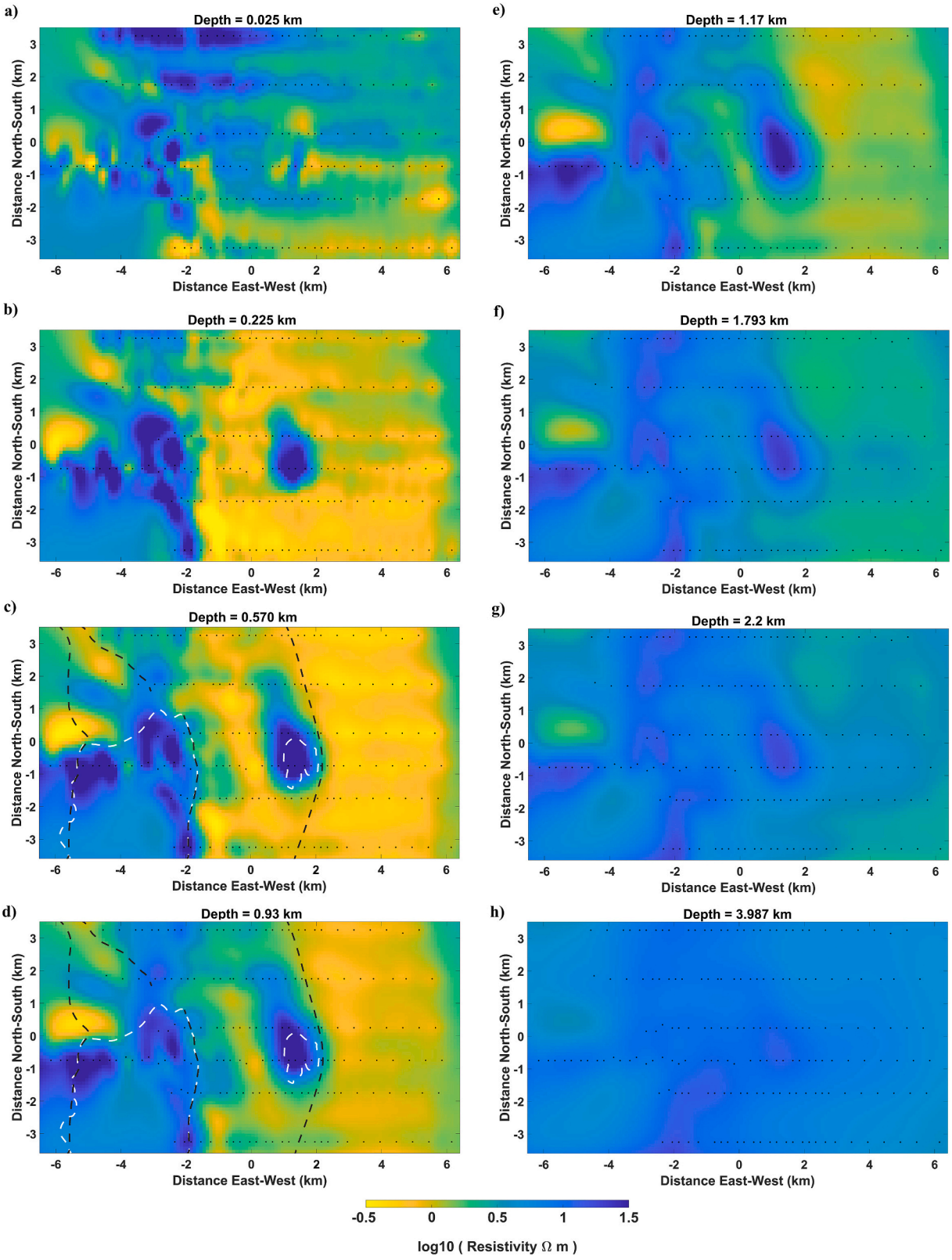

Fig. 11. Horizontal slices at different depths through the preferred 3D electrical resistivity model (full impedance tensor). Panels c and d are annotated with the approximate surface locations of faults (black lines) and salt diapirs (white lines). Note that there is limited resolution where the site distribution is not dense.

indicate a significant influence of subsurface tectonic structures. The alignment of the diapirs along a specific azimuth suggests control by an active fault system or pre-existing structural boundaries. According to Filbandi Kashkouli et al. (2025), extensional tectonics and active strike-slip faults in the region have played a primary role in the positioning and orientation of diapirs. Their study demonstrates that salt migration and diapir localization have been guided along preferential pathways created by normal and strike-slip fault zones.

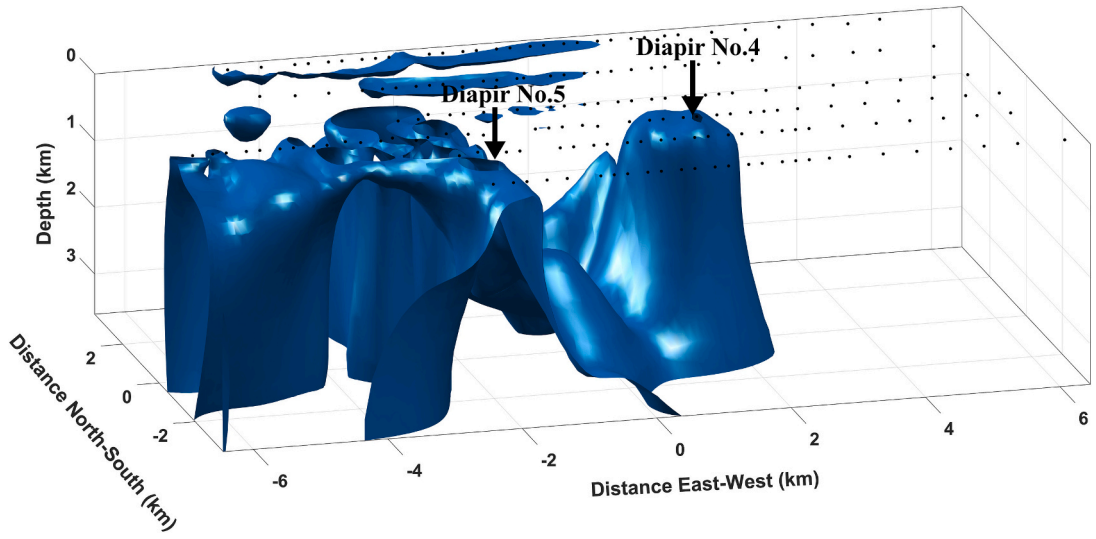

Fig. 12. A 3D perspective view of a 8 Ωm isosurface highlighting the structure of the high resistivity features, which are attributed to the salt diapirs to the east and the basement rock at depth and to the west. The black circles show the MT measurement locations at the surface.

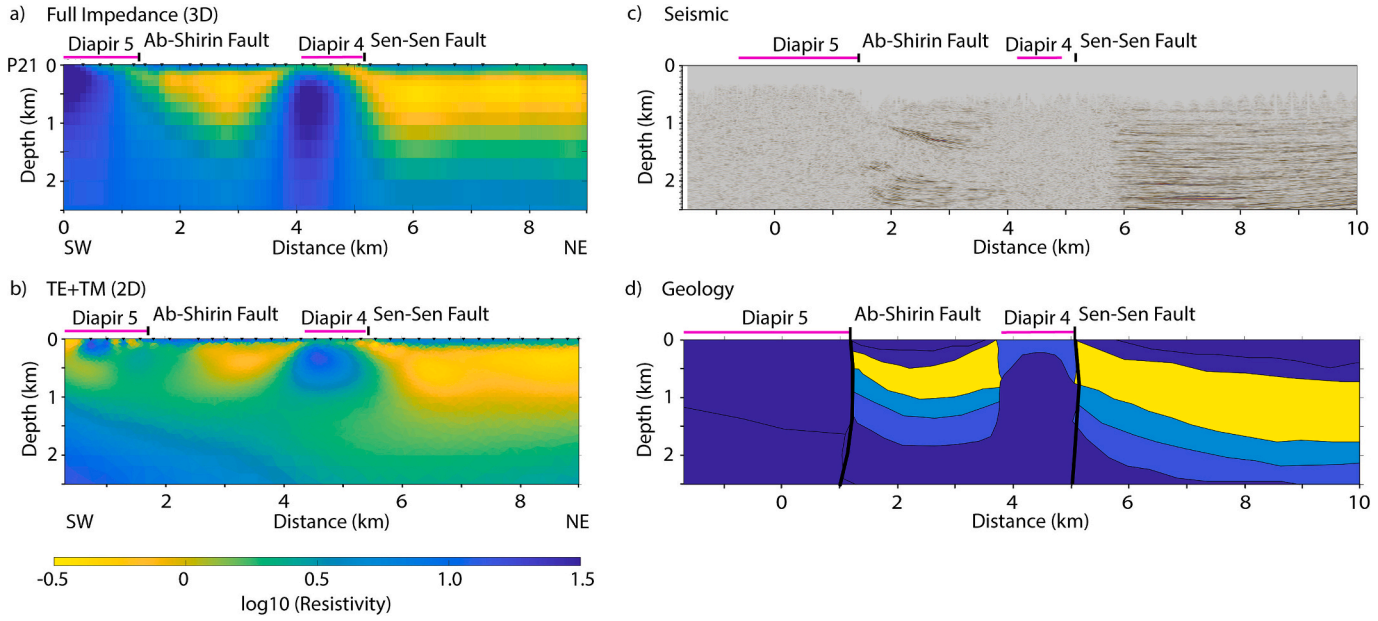

Fig. 13. Comparison of electrical resistivity models with seismic data along profile 21. (a) 3D electrical resistivity model generated from MT impedance data in this paper. (b) 2D electrical resistivity from Filbandi Kashkouli et al. (2025). (c) Seismic data along the same line (Filbandi Kashkouli et al., 2025). (d) A simplified structural section is shown for reference, with colors indicating expected electrical resistivities, based on the geological cross section that crosses the array (see Fig. 1).

In particular, Diapir No. 4 appears to have formed within a compressional zone induced by right-lateral strike-slip fault systems. This diapir is situated in a region where fault interactions have led to stress accumulation, promoting focused salt ascent. Moreover, the Sen-Sen Fault on the eastern boundary of Diapir No. 4 acts as a structural elevator, facilitating the upward movement of the salt body. These observations underscore the critical role of fault systems in controlling the emplacement and evolution of salt diapirs in this area. Additionally, Diapir No. 5 is strongly influenced by the Ab-Shirin thrust fault. This thrust structure has generated a compressive environment conducive to diapir formation. The concentration of stress and deep-seated displacements along this fault likely created favorable conditions for salt mobilization and vertical intrusion in this location.

5.3. Comparison of 3D modeling results with seismic data

Comparing structural features obtained from different geophysical methods—which are based on distinct physical parameters and, consequently, different rock properties—can enhance subsurface interpretation. Electrical resistivity and seismic velocity frequently exhibit clear correlations, even over large scales (e.g. Zhdanov et al., 2011; Takam Takougang et al., 2015; Cordell et al., 2020; Comeau et al., 2022; Long et al., 2020; Zhou et al., 2025). Owing to the distinct physical principles underlying various geophysical methods, evaluating their respective sensitivities is essential for meaningful model comparison (e.g. Schnaidt and Heinson, 2015; Unsworth et al., 2023).

Fig. 13 presents seismic reflection data along profile 21 (Filbandi Kashkouli et al., 2025). Moreover, the seismic data has only been able to

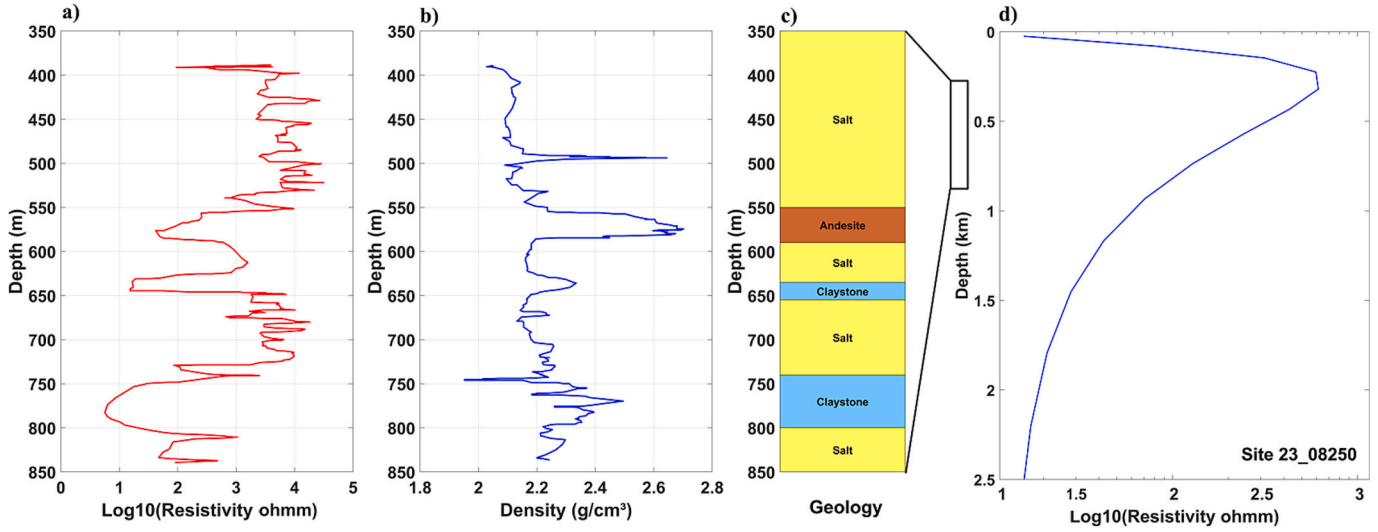

Fig. 14. Comparison between well log data and an MT sounding. Borehole log data for (a) resistivity and (b) density, along with (c) their geological interpretation. The direct measurements show much heterogeneity. (d) An MT sounding extracted from a column of the 3D electrical resistivity model below station 23_08250, near the borehole. The borehole data have been smoothed using a Savitzky–Golay filter. The 3D model shows a high resistivity zone (approximately 500 m depth) corresponding to the upper salt layers, followed by lower resistivity values, possibly associated with clay-rich or saline-saturated formations.

delineate the eastern and western flanks of the diapirs, but have failed to determine their roof and depth. This is typical and is a known limitation (e.g., Avdeeva et al., 2012). The 2D electrical resistivity model presented by Filbandi Kashkouli et al. (2025) could provide a general view of the layering and geometry of diapirs No. 4 and 5; however, it was not sufficient for fully resolving their geometry. In contrast, 3D (full impedance) electrical resistivity model has more accurately defined the geometric features—namely the roof, flanks, and depth—of the diapirs. Furthermore, it has more clearly revealed the stratification of different geological formations.

5.4. Comparison of 3D modeling results with well-logging data

To further evaluate the 3D model, we compared the results with data from the only borehole drilled in the study area. The borehole is located near station 23_08250. Fig. 14 presents the borehole-derived resistivity and density logs, along with the resistivity sounding extracted from the 3D inversion model.

The resistivity values obtained from borehole logging exhibit significant fluctuations. Notably, high resistivity values are observed in the intervals between 400 and 550 m and 650–730 m depth, which are associated with the presence of dry salt. In other intervals, the resistivity values are likely reduced due to the presence of clay-rich units. The density values vary from 1.9 g/cm^3 to 2.7 g/cm^3. A sharp increase in density is observed between 550 and 600 m depth, which corresponds to the presence of an andesite layer. In zones containing salt, the density is relatively low, around 2.1 g/cm^3.

Fig. 14d presents a vertical electrical resistivity sounding extracted from the 3D model below station 23_08250. It illustrates the general trend of resistivity variations with depth down to approximately 2.5 km. It also emphasizes that the 3D inversion approach does not attempt to resolve sharp resistivity boundaries, but rather smooth structure to fit the data (e.g., Wang et al., 2022).

The electrical resistivity sounding indicates a high resistivity in the near-surface layers at depths between 250 and 370 m, consistent with the presence of dry salt layers. With increasing depth, a decrease in resistivity is observed. This is attributed to the transition into clay-rich units or rocks saturated with saline water. A comparison between the 3D electrical resistivity model and borehole electrical resistivity data reveals that, despite the limited resolution and smoothing of the 3D model, its general trend aligns well with the borehole results. This correlation validates the geophysical modeling and highlights its capability to identify subsurface salt domes. This comparison highlights the value of integrating or constraining multiple data sets to enhance subsurface interpretation and it also shows the challenge to do that with data of different sensitivities.

6. Conclusion

This study aimed to develop a comprehensive 3D electrical resistivity model to better understand the structure and geometry of the Shurab salt diapirs in northwestern Central Iran. To achieve the objectives of this study, MT data from a total of 183 measurement sites were analyzed. Data analysis in the form of PT and RPT revealed the presence of a complex subsurface features embedded in a layered background structure. Subsequently, 3D electrical resistivity models were generated through inversion of the MT data. To ensure a robust modeling outcome, a variety of tests were conducted using different parameters, datasets, and approaches.

Interpretation of the electrical resistivity model was aided by a geological section and borehole data. The model reveals compelling evidence for structural connectivity and shared origins among the salt diapirs. The observed continuity suggests that the diapirs may originate from a common source layer, mobilized through lateral salt flow influenced by regional tectonics. The narrow and vertically concentrated roots of the diapirs indicate focused upward migration likely guided by pre-existing fractures and fault zones. They may also reflect conductive faulted regions or fluid pathways, hinting at potential hydraulic connectivity between the diapirs. Tectonic analysis reveals that Diapir No. 4 developed within a compressional zone associated with right-lateral strike-slip faulting, with the Sen-Sen Fault on its eastern boundary acting as a structural elevator aiding salt ascent. Furthermore, Diapir No. 5 is strongly influenced by the Ab-Shirin thrust fault, which provides the compressional conditions necessary for salt intrusion. Collectively, these findings underscore the dominant role of active tectonics not only in salt mobilization but also in shaping the geometry, alignment, and interconnection of the diapiric system.

CRediT authorship contribution statement

Mohammad Filbandi Kashkouli: Writing – review & editing, Writing – original draft, Visualization, Software, Methodology, Formal

analysis, Conceptualization. **Matthew J. Comeau:** Writing – review & editing, Visualization, Validation, Software, Methodology, Formal analysis, Supervision. **Abolghasem Kamkar-Rouhani:** Writing – review & editing, Resources. **Alireza Arab-Amiri:** Writing – review & editing.

Declaration of competing interest

The authors declare that they have no known competing financial interests or personal relationships that could have appeared to influence the work reported in this paper.

Acknowledgements

We thank G. Egbert, A. Kelbert, N. Meqbel, and collaborators for the ModEM 3D MT inversion code. Phase tensor and resistivity phase tensor computations were performed with the FFMT toolbox (Castro et al., 2020). Iran Gas Engineering and Development Company provided the data. Questions on the study can be addressed to M. F. Kashkouli at kashkoulimohammad@gmail.com.

Appendix A. Supplementary data

Supplementary data to this article can be found online at https://doi.org/10.1016/j.pepi.2025.107457.

Data availability

The authors do not have permission to share data.

References

Aleksanova, E.D., Alekseev, D.A., Suleimanov, A.K., Yakovlev, A.G., 2009. Magnetotelluric studies in salt-dome tectonic settings in the pre-Caspian depression. First Break 27 (3). https://doi.org/10.3997/1365-2397.27.1297.28836.

Alsop, G.I., Archer, S., Hartley, A.J., Grant, N., Hodgkinson, R. (Eds.), 2012. Salt Tectonics, Sediments and Prospectivity. Geological Society, Bath, England.

Arian, M., 2012. Clustering of diapiric provinces in the Central Iran Basin. Carbonates Evaporites 27 (1), 9–18. https://doi.org/10.1007/s13146-011-0079-9.

Avdeeva, A., Avdeev, D., Jegen, M., 2012. Detecting a salt dome overhang with magnetotellurics: 3D inversion methodology and synthetic model studies. GEOPHYSICS 77 (4), E251–E263. https://doi.org/10.1190/geo2011-0167.1.

Baikpour, S., Motiei, H., Najafzadeh, K., 2016. Geological and geophysical study of salt diapirs for hazardous waste disposal. Int. J. Environ. Sci. Technol. 13 (8), 1951–1972. https://doi.org/10.1007/s13762-016-1036-x.

Berberian, M., King, G.C.P., 1981. Towards a paleogeography and tectonic evolution of Iran. Can. J. Earth Sci. 18 (2), 210–265. https://doi.org/10.1139/e81-019.

Berdichevsky, M.N., Dmitriev, V.I., 2008. Models and Methods of Magnetotellurics. Springer Berlin Heidelberg. https://doi.org/10.1007/978-3-540-77814-1.

Bibby, H.M., Caldwell, T.G., Brown, C., 2005. Determinable and non-determinable parameters of galvanic distortion in magnetotellurics. Geophys. J. Int. 163 (3), 915–930. https://doi.org/10.1111/j.1365-246x.2005.02779.x.

Booker, J.R., 2013. The Magnetotelluric phase tensor: a critical review. Surv. Geophys. 35 (1), 7–40. https://doi.org/10.1007/s10712-013-9234-2.

Bostick, F.X., 1977. A simple almost exact method of MT analysis: Workshop on Electrical Methods in Geothermal Exploration, U.S. Geol. Sur. Contract. No. 14080001–8-359. In: Workshop on Electrical Methods in Geothermal Exploration, University of Utah Rpt., U.S.G.S contact 14-08-0001-g-359. Ward S.H., ed (183pp).

Brown, C., 2016. Magnetotelluric tensors, electromagnetic field scattering and distortion in three-dimensional environments. J. Geophys. Res. Solid Earth 121, 7040–7053. https://doi.org/10.1002/2016JB013035.

Caldwell, T.G., Bibby, H.M., Brown, C., 2004. The magnetotelluric phase tensor. Geophys. J. Int. 158 (2), 457–469. https://doi.org/10.1111/j.1365-246x.2004.02281.x.

Castro, C.D., Hering, P., Junge, A., 2020. FFMT: A MATLAB-based toolbox for Magnetotellurics (MT). Unpublished. https://doi.org/10.13140/RG.2.2.12465.92007.

Comeau, M.J., Becken, M., Kuvshinov, A.V., Demberel, S., 2021. Crustal architecture of a metallogenic belt and ophiolite belt: implications for mineral genesis and emplacement from 3-D electrical resistivity models (Bayankhongor area, Mongolia). Earth Planets Space 73 (1). https://doi.org/10.1186/s40623-021-01400-9.

Comeau, M.J., Becken, M., Kuvshinov, A., 2022. Imaging the whole-lithosphere architecture of a mineral system—geophysical signatures of the sources and pathways of ore-forming fluids. Geochem. Geophys. Geosyst. 23 (8). https://doi.org/10.1029/2022GC010379.

Cordell, D., Unsworth, M.J., Lee, B., Díaz, D., Bennington, N.L., Thurber, C.H., 2020. Integrating magnetotelluric and seismic images of silicic magma systems: a case study from the Laguna del Maule volcanic field, Central Chile. J. Geophys. Res. Solid Earth 125 (11). https://doi.org/10.1029/2020jb020459.

Davison, I., Jones, I.F., Waltham, D., 2013. Seismic imaging of salt diapirs: Problems and pitfalls. In: 13th International Congress of the Brazilian Geophysical Society & EXPOGEF, Rio de Janeiro, Brazil, 26–29 August 2013, pp. 1332–1336. https://doi.org/10.1190/sbgf2013-274.

den Boer, E., Eikelboom, J., van Driel, P., Watts, D., 2000. Resistivity imaging of shallow salt with magnetotellurics as an aid to prestack depth migration. First Break 18 (1), 19–26. https://doi.org/10.1046/j.1365-857 2397.2000.181047.x.

Egbert, G.D., Kelbert, A., 2012. Computational recipes for electromagnetic inverse problems. Geophys. J. Int. 189 (1), 251–267. https://doi.org/10.1111/j.1365-246X.2011.05347.x.

Filbandi Kashkouli, M., Kamkar-Rouhani, A., Arab-Amiri, A., Comeau, M.J., Esmaeili Oghaz, H., 2025. The subsurface structure of salt diapirs revealed with electrical resistivity models in the Shurab area, Central Iran. Tectonophysics 909, 230774. https://doi.org/10.1016/j.tecto.2025.230774.

Furrer, M.A., Suder, P.A., 1955. The Oligo–Miocene marine formation in the Qom region (Iran). In: 4th World Petroleum Congress. World Petroleum Congress, 1–1.

Gou, Y., Liu, M., 2024. Active and passive salt diapirs: a numerical study. Geophys. J. Int. 239 (1), 621–636. https://doi.org/10.1093/gji/ggae284.

Grayver, A., Tietze, K., Ritter, O., 2013. RMS–Rather Meaningless Simplification? Proceedings of the 25th Schmucker-Weidelt Kolloquium für Elektromagnetische Tiefenforschung, 23–27 September 2013, Rahrbach, Germany, pp. 31–35.

Henke, C.H., Krieger, M.H., Strack, K., Zerilli, A., 2020. Subsalt imaging in northern Germany using multiphysics (magnetotellurics, gravity, and seismic). Interpretation 8 (4), SQ15–SQ24. https://doi.org/10.1190/int-2020-0026.1.

Hering, P., Brown, C., Junge, A., 2019. Magnetotelluric apparent resistivity tensors for improved interpretations and 3-D inversions. J. Geophys. Res. Solid Earth 124 (8), 7652–7679. https://doi.org/10.1029/2018jb017221.

Hersir, G.P., Arnason, K., Vilhjalmsson, A.M., 2013. 3D inversion of magnetotelluric (MT) resistivity data from Krysuvık high temperature geothermal area in SW Iceland. In: Proceedings of the 38th Workshop on Geothermal Reservoir Enineering. Stanford Univ, Stanford, 14 pp.

Jackson, M.P.A., Hudec, M.R., 2017. Salt tectonics. https://doi.org/10.1017/9781139003988.

Jackson, C.A.-L., Jackson, M.P.A., Hudec, M.R., Rodriguez, C.R., 2015. Enigmatic structures within salt walls of the Santos Basin—part 1: geometry and kinematics from 3D seismic reflection and well data. J. Struct. Geol. 75, 135–162. https://doi.org/10.1016/j.jsg.2015.01.010.

Jones, A.G., 1983. On the equivalence of the "Niblett" and "Bostick" transformation in the magnetotelluric method. J. Geophys. 53, 72–73.

Jones, I.F., Davison, I., 2014. Seismic imaging in and around salt bodies. Interpretation 2 (4), SL1–SL20. https://doi.org/10.1190/int-2014-0033.1.

Kelbert, A., Meqbel, N., Egbert, G.D., Tandon, K., 2014. ModEM: a modular system for inversion of electromagnetic geophysical data. Comput. Geosci. 66, 40–53. https://doi.org/10.1016/j.cageo.2014.01.010.

Key, K.W., Constable, S.C., Weiss, C.J., 2006. Mapping 3D salt using the 2D marine magnetotelluric method: case study from Gemini Prospect, Gulf of Mexico. GEOPHYSICS 71 (1), B17–B27. https://doi.org/10.1190/1.2168007.

Leveille, J.P., Jones, I.F., Zhou, Z.-Z., Wang, B., Liu, F., 2011. Subsalt imaging for exploration, production, and development: a review. GEOPHYSICS 76 (5), WB3–WB20. https://doi.org/10.1190/geo2011-0156.1.

Lewis, S., Holness, M., 1996. Equilibrium halite-H2O dihedral angles: high rock-salt permeability in the shallow crust? Geology 24 (5), 431–434. https://doi.org/10.1130/0091-7613(1996)024<0431:EHHODA>2.3.CO;2.

Long, M.D., Benoit, M.H., Evans, R.L., Aragon, J.C., Elsenbeck, J., 2020. The MAGIC experiment: a combined seismic and magnetotelluric deployment to investigate the structure, dynamics, and evolution of the Central Appalachians. Seismol. Res. Lett. 91 (5), 2960–2975. https://doi.org/10.1785/0220200150.

Montazeri, M., Boldreel, L.O., Uldall, A., Nielsen, L., 2020. Improved seismic interpretation of a salt diapir by utilization of diffractions, exemplified by 2D reflection seismics, Danish sector of the North Sea. Interpretation 8 (1), T77–T88. https://doi.org/10.1190/int-2018-0190.1.

Moradi, M., Oskooi, B., Pushkarev, P., Smirnov, M., Esmaeili Oghaz, H., 2019. Cooperative inversion of magnetotelluric and seismic data on Shurab diapirs in Central Iran. Environ. Earth Sci. 78 (11). https://doi.org/10.1007/s12665-019-8342-9.

Morley, C.K., Kongwung, B., Julapour, A.A., Abdolghafourian, M., Hajian, M., Waples, D., Warren, J., Otterdoom, H., Srisuriyon, K., Kazemi, H., 2009. Structural development of a major late Cenozoic basin and transpressional belt in Central Iran: the Central Basin in the Qom-Saveh area. Geosphere 5 (4), 325–362. https://doi.org/10.1130/ges00223.1.

Mrlina, J., Beránek, R., 2024. Impact of salt diapir geometry and caprock composition on gravity survey results. J. Struct. Geol. 186, 105214. https://doi.org/10.1016/j.jsg.2024.105214.

Niblett, E.R., Sayn-Wittgenstein, C., 1960. Variation of electrical conductivity with depth by the magnetotelluric method. Geophysics 25, 998–1008. https://doi.org/10.1190/1.1438799.

Pinto, V., Casas, A., Rivero, L., Torné, M., 2005. 3D gravity modeling of the Triassic salt diapirs of the Cubeta Alavesa (northern Spain). Tectonophysics 405 (1–4), 65–75. https://doi.org/10.1016/j.tecto.2005.05.010.

Reuter, M., Piller, W.E., Harzhauser, M., Mandic, O., Berning, B., Rögl, F., Kroh, A., Aubry, M.-P., Wielandt-Schuster, U., Hamedani, A., 2007. The Oligo-/Miocene Qom Formation (Iran): evidence for an early Burdigalian restriction of the Tethyan

Seaway and closure of its Iranian gateways. Int. J. Earth Sci. 98 (3), 627–650. https://doi.org/10.1007/s00531-007-0269-9.
Robertson, K., Thiel, S., Meqbel, N., 2020. Quality over quantity: on workflow and model space exploration of 3D inversion of MT data. Earth Planets Space 72. https://doi.org/10.1186/s40623-019-1125-4.
Rubinat, M., Ledo, J., Roca, E., Rosell, O., Queralt, P., 2010. Magnetotelluric characterization of a salt diapir: a case study on Bicorb–Quesa Diapir (Prebetic Zone, SE Spain). J. Geol. Soc. Lond. 167 (1), 145–153. https://doi.org/10.1144/0016-76492009-029.
Santolaria, P., Casas-Sainz, A.M., Soto, R., Pinto, V., Casas, A., 2014. The naval diapir (southern Pyrenees): geometry of a salt wall associated with thrusting at an oblique ramp. Tectonophysics 637, 30–44. https://doi.org/10.1016/j.tecto.2014.09.008.
Schnaidt, Sebastian, Heinson, Graham, 2015. Bootstrap resampling as a tool for uncertainty analysis in 2-D magnetotelluric inversion modelling. Geophys. J. Int. 203 (1), 92–106. https://doi.org/10.1093/gji/ggv264.
Sonder, P.A., 1954. The Tertiary of the Qum-Shurab Area. Iran Oil Company Geological Report, p. 75.
Stefanescu, M., Dicea, O., Tari, G., 2000. Influence of extension and compression on salt diapirism in its type area, East Carpathians Bend area, Romania. Geol. Soc. 174 (1), 131–147. https://doi.org/10.1144/gsl.sp.1999.174.01.08.
Takam Takougang, E.M., Harris, B., Kepic, A., Le, C.V.A., 2015. Cooperative joint inversion of 3D seismic and magnetotelluric data: with application in a mineral province. GEOPHYSICS 80 (4), R175–R187. https://doi.org/10.1190/geo2014-0252.1.
Teofilo, G., Festa, V., Sabato, L., Spalluto, L., Tropeano, M., 2016. 3D modelling of the Tremiti salt diapir in the Gargano offshore (Adriatic Sea, southern Italy): constraints in the Tremiti structure development. Ital. J. Geosci. 135 (3), 474–485. https://doi.org/10.3301/ijg.2015.40.
Tietze, K., Ritter, O., 2013. Three-dimensional magnetotelluric inversion in practice—the electrical conductivity structure of the San Andreas Fault in Central California. Geophys. J. Int. 195 (1), 130–147. https://doi.org/10.1093/gji/ggt234.
Tietze, K., Thiel, S., Brand, K., Heinson, G., 2023. Comparative 3D inversion of magnetotelluric phase tensors and impedances reveals electrically anisotropic base of Gawler Craton, South Australia. Explor. Geophys. 55 (5), 575–601. https://doi.org/10.1080/08123985.2023.2281615.
Unsworth, M., Rondenay, S., 2012. Mapping the distribution of fluids in the crust and lithospheric mantle utilizing geophysical methods. Lecture Notes Earth Syst. Sci. 535–598. https://doi.org/10.1007/978-3-642-28394-9_13.
Unsworth, M., Comeau, M.J., Diaz, D., Brasse, H., Heit, B., Favetto, A., et al., 2023. Crustal structure of the Lazufre volcanic complex and the southern Puna from 3-D inversion of magnetotelluric data: implications for surface uplift and evidence for melt storage and hydrothermal fluids. Geosphere 19 (5). https://doi.org/10.1130/GES02506.1, 1210–1044.
Van Gent, H., Urai, J.L., de Keijzer, M., 2011. The internal geometry of salt structures – a first look using 3D seismic data from the Zechstein of the Netherlands. J. Struct. Geol. 33 (3), 292–311. https://doi.org/10.1016/j.jsg.2010.07.005.
Wang, T., Ma, G., et al., 2022. Evidence for the superposition of tectonic systems in the Northern Songliao Block, NE China, revealed by a 3-D electrical resistivity model. JGR 127 (4). https://doi.org/10.1029/2021JB022827.
Warsitzka, M., Kley, J., Kukowski, N., 2015. Analogue experiments of salt flow and pillow growth due to basement faulting and differential loading. Solid Earth 6 (1), 9–31. https://doi.org/10.5194/se-6-9-2015.
Weaver, J.T., 1994. Mathematical Methods for GeoElectromagnetic Induction. Wiley, New York, p. 316.
Wu, L., Trudgill, B.D., Kluth, C.F., 2016. Salt diapir reactivation and normal faulting in an oblique extensional system, Vulcan sub-basin, NW Australia. J. Geol. Soc. Lond. 173 (5), 783–799. https://doi.org/10.1144/jgs2016-008.
Zhdanov, M.S., Wan, L., Gribenko, A., Čuma, M., Key, K., Constable, S., 2011. Large-scale 3D inversion of marine magnetotelluric data: case study from the Gemini prospect, Gulf of Mexico. GEOPHYSICS 76 (1), F77–F87. https://doi.org/10.1190/1.3526299.
Zhou, H., Guo, R., Hu, Z., Wei, W., Li, M., Yang, F., Xu, S., Shi, Y., 2025. Super-resolution magnetotelluric data inversion with seismic texture constraint. GEOPHYSICS 90 (3), WA153–WA168. https://doi.org/10.1190/geo2024-0113.1.